Nonlinear Quantum Mechanics

Björn Birnir

Abstract We show that the nonlinear bifurcations found by simulations in single quantum wells in the terahertz regime [5, 6, 25] also occur in semiconductor superlattices (SSLs) in the gigahertz range [2, 3, 11]. The only exception is the second Hopf bifurcation to quasi-periodic orbits on a torus. The advantage of experiments on SSLs in the gigahertz range is that the experiments can be conducted at room temperature and a chaotic oscillator due to the random dressing of a period two-orbit has already been measured [31, 32]. We determine [42] that the route to chaos for SSLs in the sequential tunneling regime is the period doubling cascade. Shorter (10-period) superlattices are observed to exhibit faster oscillations compared with longer (50-period) ones. Two plateaus are observed as functions of the voltage bias, and intrinsically chaotic dynamics on the second plateau are possible only for shorter SSLs, while the dynamics in the first plateau contain intrinsic chaos only for longer ($N > 50$) SSLs [21].

Keywords Semiconductor · Superlattice · Nonlinear quantum systems · Quantum strange attractors · Quantum bifurcations

1 Introduction

Quantum wells are fabricated (or 'grown') from semiconductors by depositing a thin layer of one material, such as gallium arsenide $GaAs$, onto a substrate of a different material, such as aluminum gallium arsenide $AlGaAs$, followed by another layer of substrate material, so that a type of 'sandwich' geometry called a heterostructure is formed. The defining property of quantum wells is that the middle layer has a

B. Birnir (✉)
Department of Mathematics and CNLS, University of California,
Santa Barbara, CA 93106, USA
e-mail: birnir@math.ucsb.edu

B. Birnir
University of Iceland, 107, Reykjavík, Iceland

L. L. Bonilla et al. (eds.), *Coupled Mathematical Models for Physical and Biological Nanoscale Systems and Their Applications*, Springer Proceedings in Mathematics & Statistics 232, https://doi.org/10.1007/978-3-319-76599-0_1

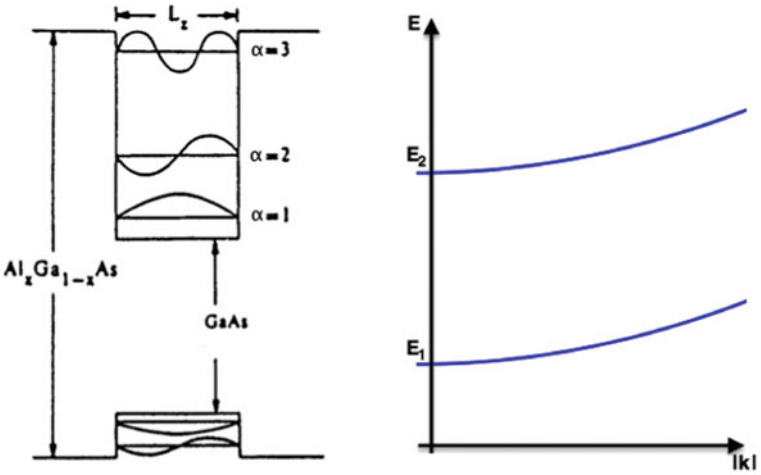

Fig. 1 Left: the conduction and valance band for a semiconductor heterostructure, showing several 'bare' electron and hole subbands (states). Right: the parabolic subbands of the energies $E_{k_x k_y \alpha}$ of the envelope wavefunctions ξ_α

significantly smaller band gap than the substrate layers, and has thickness of the same order as the de Broglie wavelength of the electron. This causes an electron occupying the conduction band of the middle layer to be confined to move freely in only two dimensions, while motion in the third dimension is only possible via transitions between quantized energy levels, called 'subbands', see Fig. 1. These wells can be populated by a density of electrons by a process called doping and this makes them ideal quantum systems for the study of nonlinear effects.

The success of nonlinear dynamical systems theory in the late 20th century, see Guckenheimer and Holmes [28], and its application in the sciences and engineering, see for example Birnir [9], lead to the conjecture that similar phenomena could be found in quantum systems. In semi-classical systems nonlinear dynamics and bifurcations of coherent solutions (solitons) have been shown to exist [7, 8, 27, 35], so it is not unreasonable to expect nonlinearity in some quantum systems far from the semi-classical limit. In the late 1990s and early 2000s, Galdrikian, Batista, Birnir et al. [5, 6, 25] studied intersubband transitions of doped quantum wells. They developed computational methods for determining the coherent states of the electron gas in an oscillating external electric field. It was found that the density matrix equations of motion were nonlinear due to the interactions of the electron gas and that these nonlinearities could be enhanced by fabricating quantum wells with certain asymmetries, so that the lowest-lying subband levels were close to one another in energy. For sufficiently nonlinear wells, it was predicted that the wells would exhibit a bistable response as the terahertz power of the electric field (laser) was ramped up and then down. For strong enough terahertz fields, period-doubling bifurcations leading to a period-doubling cascade were predicted. Galdrikian, Batista, Birnir et al.

[5, 6, 25] developed this nonlinear theory of semiconductor quantum wells, typically made out of $GaAs$ and $Al_zGa_{1-z}As$ and populated by the technique of doping, where material providing electrons is deposited close to the well structure, see Heyman et al. [29, 30]. The nonlinearity was introduced through the Hartree and Hartree-Fock local density approximation where a system of n-interacting electrons is replaced by a system of n-noninteracting electrons in a different (Hartree) potential. This latter view leads to the quantum mechanical system of coherent electron states. These states satisfy a Schrödinger equation where the potential depends on several parameters and when these parameters change the coherent electron states can bifurcate.

2 The Local Density Approximation

We now briefly describe the steps involved in obtaining the nonlinear quantum system describing the coherent electron states and their bifurcations. It is possible to add donor-type dopants at the interfaces of the middle layer with the substrate layers, so that a two-dimensional electron gas will occupy the well. In order to describe such a system theoretically, we take advantage of the fact that all the materials involved exhibit a periodic crystal lattice structure, which constrains the allowed electronic states and leads to a set of semiconductor Bloch equations. Assuming that the electron gas is not too dense, we make an effective mass approximation and work with a simplified model that will be discussed below. The starting point is the Heisenberg equation for the electron operator

$$i\hbar\frac{\partial\psi}{\partial t} = [\psi, H].$$

Let the x- and z-coordinates parameterize the lateral and growth directions of the heterostructure, respectively. Here x is a two-dimensional coordinate parameterizing both the direction of lateral and the transverse direction. Since the wavelength of the laser drive is much longer than the width of the quantum well, the vertical field will be coupled to the electrons in the active region with the dipole approximation. In the effective mass approximation, the mean field Hamiltonian including the vertical field Fz (which falls off rapidly outside the active region) is

$$H(t) = \int \psi^{\dagger}(x,z,t)[\frac{\hbar^2}{2m}\nabla^2 + v(x,z) + w(x,z,t) - ezF(x,t)]\psi(x,z,t)\,d^2x dz,$$

where v and w are the time-independent and time-dependent parts of the electric potential, respectively, e is the electron charge and m is the effective mass. The electric potential is coupled to the electron density n by Poisson's equation

$$\nabla^2[v(x,z) + w(x,z,t)] = -\frac{e}{\epsilon}n(x,z,t)$$

where

$$n(x, z, t) = \langle \psi^\dagger(x, z, t)\psi(x, z, t)\rangle,$$

is the electron density. The electron operator is expressed as

$$\psi(x, z, t) = \sum_\alpha \int e^{ik\cdot x}\xi_\alpha(z)a_{k\alpha}(t)\,\frac{d^2k}{2\pi} \tag{1}$$

where the envelope wavefunctions $\xi_\alpha(z)$ form a complete orthonormal basis. If the active region is filled and the bias voltage is zero (i.e. the electron density is uniform), then the self-consistent envelope wavefunctions may be calculated in the same manner as in Galdrikian, Batista and Birnir [5, 6, 25].

3 Homogeneous Quantum Wells

The theory of homogenous quantum wells with the local density approximation consists of the following steps. We discretize the integral in Eq. (1) and write the electron operator as

$$\psi(x, y, z) = A^{-1/2} \sum_{k_x,k_y,\alpha} a_{k_xk_y\alpha}\, e^{ik\cdot x}\, \xi_\alpha(z),$$

where A is a constant. The envelope wavefunctions obey the time-independent Schrodinger equation

$$\left\{-\frac{\hbar^2}{2m}\frac{\partial^2}{\partial z^2} + v(z)\right\}\xi_\alpha(z) = E_\alpha\xi_\alpha(z), \tag{2}$$

with the energies lying in parabolic subbands

$$E_{k_xk_y\alpha} = \frac{\hbar^2}{2m}(k_x^2 + k_y^2) + E_\alpha, \tag{3}$$

see Fig. 1. The envelope wave functions satisfy vanishing boundary conditions at the sides of the well, which is a good proxy for a vanishing boundary conditions at $z = \pm\infty$, see [5, 25]. The self-consistent potential is determined by Poisson equation

$$\frac{\partial^2}{\partial z^2}v(z) = -\frac{e^2}{\varepsilon}n(z). \tag{4}$$

The local density (or Hartree) approximation is implemented by use of the partition function that yields the relationship between the chemical potential μ, sheet density N_s and subband energies E_α, giving the thermal weights w_α

$$N_s = \frac{m}{\pi\hbar^2\beta}\sum_\alpha \log\left\{1 + e^{-\beta(E_\alpha-\mu)}\right\} \equiv \frac{m}{\pi\hbar^2\beta}\sum_\alpha w_\alpha,$$

where $\beta = 1/T$, T being temperature. Then the electron density can be expressed as

$$n(z) = \sum_\alpha w_\alpha |\xi_\alpha(z)|^2. \tag{5}$$

4 The Hartree Iteration

The potential v is determined by a Hartree iteration:

1. Solve Schrödinger equation (2) for $\{\xi_\alpha(z), E_\alpha\}$.
2. Determine $\{\mu, w_\alpha\}$ from $\{N_s, E_\alpha\}$ and update $n(z)$ in (5).
3. Solve Poisson's equation and update $v(z)$ in (4).
4. Repeat until the iteration has converged.

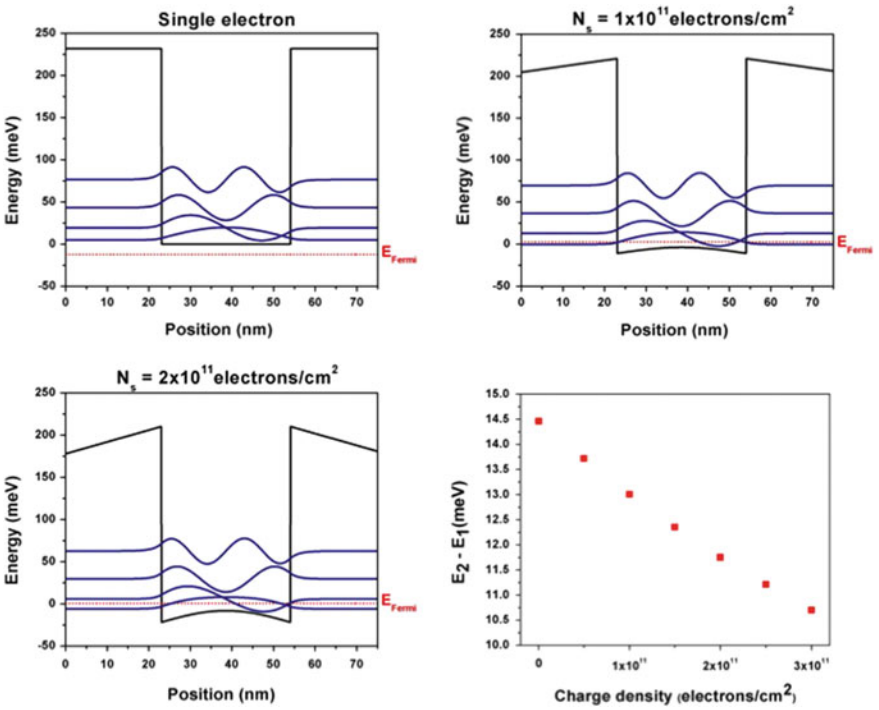

Fig. 2 The first few energy states, the shape of the potential and the Fermi energy for different doping levels and the energy difference $E_2 - E_1$ between the first and second state as a function of the charge density

Figure 2, shows the first few energy states, the shape of the potential and the Fermi energy for different doping levels and the energy difference between the first and second state as a function of the charge density.

5 Intersubband Absorption

The nonlinear effects due to the electron density in the quantum wells have been understood and measured since the mid 1990s. The intersubband absorption when the quantum well is illuminated by an auxiliary laser, can be simulated and measured. The simulations were developed by Zalużny [49, 50] and the experiments were done by Craig et al. [19]. The incoming radiation first builds up a charge in the quantum well, this is a Stark effect and corresponds to a redshift of the absorption frequency. However, as the incoming radiation increases the electrons in the well shield against it, this is called the depolarization shift and is a blue shift. Eventually, the depolarization shift dominates, see Fig. 3. One can also measure the relaxation times for the densities in the quantum well, namely Γ_1; the depopulation rate and Γ_2; the depolarization rate. This was also done by Craig et al. [19].

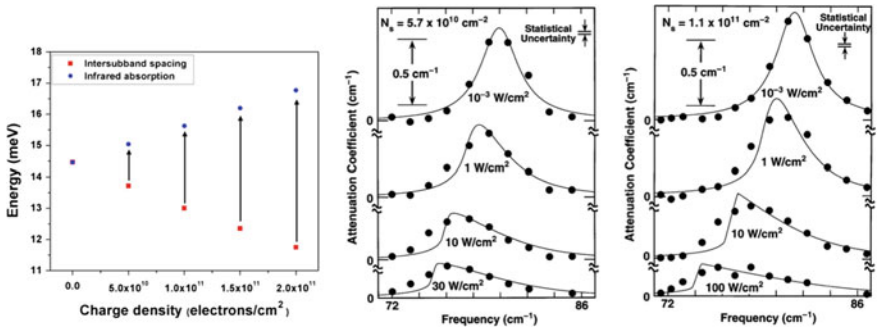

Fig. 3 The absorption frequency. The leftmost picture shows the intersubband spacing (Stark shift) and infrared absorption due to the depolarization shift, as a function of the charge density. The second and third picture show that with fixed electron (doping) density the absorption peak shifts and changes form with the amplitude of the incoming radiation. The blue shift between the two leftmost figures is the depolarization shift

6 Time-Dependent Local Density Approximation

The driving of the quantum wells with time-periodic laser fields requires the development of the time dependent version of above theory. The laser field is added to the Hamiltonian in the electric dipole approximation, this works well since the wavelength of the laser is large compared to width of the well. The intersubband absorption now occurs by collective oscillations of electrons occupying the well and the resonance is broadened and shifted away from intersubband spacing (This is the depolarization shift discussed above). Using the time-dependent Hartree (local density) approximation, we calculate the self-consistent fluctuations due to the time-periodic driving term. The time-dependent electric field $zF(t)$ now induces self-consistent fluctuations in potential $\delta v(z,t)$ and electron density $\delta n(z,t)$

$$\tilde{H}(t) = H - ezF(t) + \delta v(z,t); \qquad \frac{\partial^2}{\partial z^2}\delta v(z,t) = -\frac{e^2}{\varepsilon}\delta n(z,t).$$

These satisfy a Poisson equation with a self-consistency condition: $v(z,t) = v(z) + \delta v(z,t), n(z,t) = n(z) + \delta n(z,t)$. Then we can find a Liouville-von Neumann equation

$$\frac{\partial \rho(z,z',t)}{\partial t} = -\frac{i}{\hbar}[\tilde{H}(t), \rho(z,z',t)] - R[\rho(z,z',t)],$$

for the density matrix ρ, where R is the relaxation operator. In the final quantum mechanical dynamical system, in 4 complex dimensions, R is determined by the experimentally measured depolarization rate Γ_1 and decorrelation rate Γ_2, discussed above.

The time-dependent potential is determined by a time-dependent Hartree iteration:

1. Evolve $\rho(z,z',t)$ until a periodic response is reached.
2. Compute the electron density by the formula $n(z,t) = \rho(z,z',t)\big|_{z'=z}$.
3. Solve Poisson's equation and update $\delta v(z,t)$.
4. Repeat until converged.

7 Nonlinear Phenomena in Asymmetric Quantum Wells

Nonlinear bifurcation of the time-periodic coherent electron states were explored by the theory above. In 1996 Galdrikian and Birnir [25] found the period-doubling bifurcation of these states. In 2003 Batista et al. [6] found the Hopf bifurcation. These bifurcations were found in simulations of the above model and simulations showed the period-doubling cascade to the (Feigenbaum) strange attractor in first

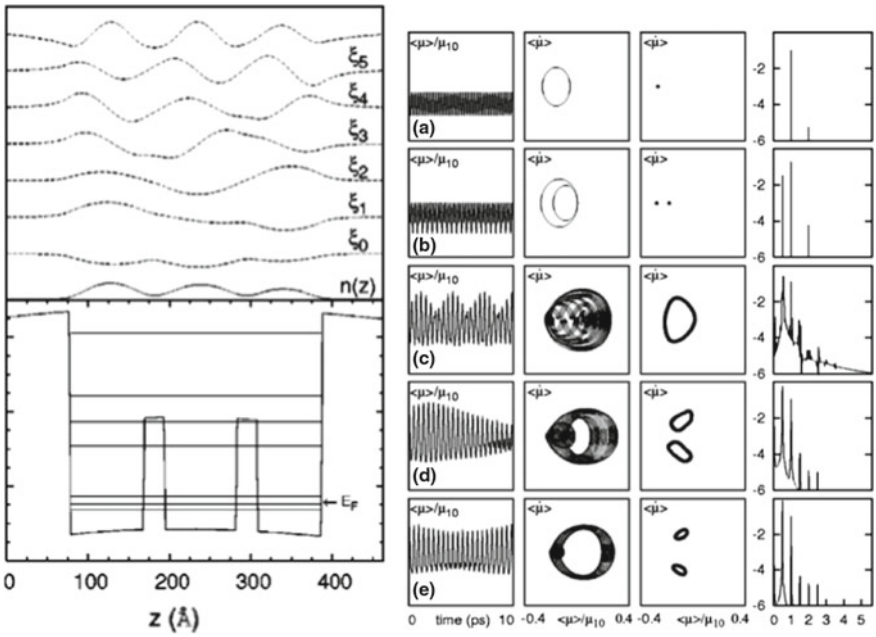

Fig. 4 Left: The asymmetric quantum well with two barriers; bottom, the corresponding eigenstates, top. Right: Time series, phase portrait, Poincaré map and power spectrum

case [25] and the quasi-periodic cascade to another strange attractor in the second case [5]. We illustrate both of these in Fig. 4, taken from Batista et al. [6]. We sample the normalized dipole momentum $\langle\mu\rangle/\mu_{10}$, $\mu = zF$ above, onto the two pertinent complex valued states, in Fig. 4, μ_{10} is a normalization. The first column in Fig. 4 is the time series of this sample. It shows if there is a simple oscillation present or if there are more oscillations superimposed. The pattern in the third row is called beating. The second column is the phase portrait, the basic mode is plotted against its derivative. Both must be sampled at the same (spatial) point. The third column is the Poincaré map, again the mode and its derivative are sampled, but now only at each period T. This is also called the stroboscopic map. A circle on the second column turns into a point in the Poincaré map. Finally the fourth column is the power spectrum or the absolute value of the Fourier transform of the solution. The fundamental frequency $\omega = 2\pi/T$ shows up as the biggest peak. Superharmonics are smaller peaks at integer valued multiples $n\omega$ of the fundamental frequency. In the first row, we see a periodic orbit, with the fundamental frequency and one superharmonic on the power spectrum. The second row shows a period doubling, we see a periodic orbit with twice the period $2T$, this is now a simple periodic orbit (two dots) on the Poincaré map in the third column, and the power spectrum now has a peak at half the frequency $\omega/2$. On the third row, we see a Hopf bifurcation in the Poincaré map, that means that we now have a torus in the phase space. The Poincaré map is

a cross section (cut) of this torus. The orbits are quasi-periodic and fill the surface of the torus. On the power spectrum we now see a new incommensurate frequency, smaller than the fundamental frequency. Then on the fourth row we see the torus period double. On the fifth row the doubled torus deforms.

8 Experimental Search by Morris and Sherwin (2011)

A thorough experimental search for the period doubling bifurcation was done by Sherwin and Morris [38], the experimental configuration is illustrated in Fig. 5. They found superharmonics that are signs of the nonlinearity but no subharmonic of the fundamental frequency. The latter is the signature of the period doubling bifurcation. Optical bistability that frequently precedes a period doubling bifurcation was not observed either. It is possible that the subharmonic signal was too weak to be observed but other possible issues include: 1. Excessive heating in the quantum well. It is possible that the laser drive ionizes the electrons by excessive heating before the subharmonic is able to form. 2. Domain formation, it is possible that domains with difference charges form in the lateral direction perpendicular to the confinement direction of the well. If this is the case these may add up and cancel or minimize the effect of the nonlinearity.

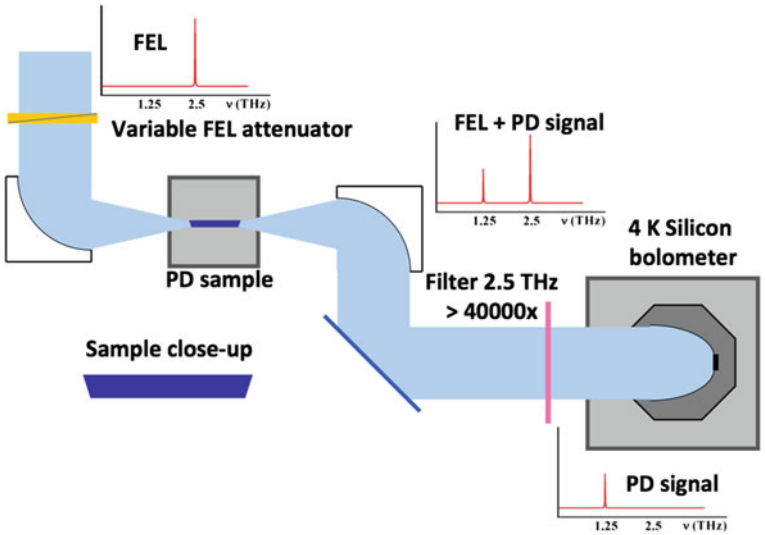

Fig. 5 The experimental setup of Morris and Sherwin (2011). FEL denotes the free-energy laser (with frequency 2.5 THz). PD denotes the period doubling. The fundamental FEL frequency is filtered out to observe the subharmonic (1.25 THz) signal

9 The Anticipated Results: The Quantum Oscillator

A natural way to strengthening the signal emitted by coherent electron states in a quantum well is to string together several quantum wells into a heterostructure called a superlattice (SL). An example is shown in Fig. 6, taken from Alvaro et al. [1].

In the proposed research we will design and simulate SLs that can be used as sources, period halvers and squeezers, random sequence generators and frequency mixers, at room temperature. Periodic, quasi-periodic and chaotic oscillations have been observed in superlattices [34, 47], at very low temperatures that require cooling with liquid nitrogen. We propose to design and simulate SLs where all these phenomena can be simulated and understood dynamically at room temperatures. The design of such SLs requires heterostructures where the background temperature is surppressed and below we will discuss the structure of such lattices. First we list the devices and dynamical phenomena that we propose to find and study:

A Source: The difference between the above analysis of the oscillations in the quantum well and the oscillations in the SL is that we drove the quantum well with an ac laser field, whereas the electron states in the SL will be driven by a dc voltage. This means that whereas we always start with a time-periodic orbit in the quantum well, in the SL we start with a steady current (stationary state). The first bifurcation we will look for is the generic Hopf bifurcation, from the stationary state, in such an SL. Here generic means that it is the bifurcation we expect to find in the SL, as the voltage bias increases, assuming it has no other symmetries. After this bifurcation we expect to find a circle in the phase portrait of the SL system (6–11), as in the first row of the second column on Fig. 4. This electron state is a *source*, namely the electron state consists of a charge, accelerated over the periodic oscillation. It will emit radiation at the frequency $\omega = 2\pi/T$, where T is the period and at its superharmonics, because of the nonlinearity of the coherent electron state. We expect to find up a 1–100 GHz source, and if we succeed, we will next try to design a terahertz source that operates at room temperatures. In fact the frequency can be tuned with the applied voltage. This would enable terahertz sources that could be put on satellites without a heavy cooling system; a great advantage. The signatures of the periodic orbit are the figures in row one on Fig. 4. They are a simple periodic oscillation in the current, a circle in the phase portrait, a fixed point (point) on the Poincaré map and a single peak at the frequency ω on the power spectrum.

A Frequency Halver and Squeezer: The second bifurcation, now starting from the periodic orbit, that we expect to find in the SL, is the period-doubling bifurcation on row two in Fig. 4. Now the periodic orbit has period twice that of the original periodic orbit, so the frequency gets cut in half: $\omega \to \omega/2$. This has many applications, the signal can be read at lower frequency where the noise may be reduced, it can be used to make squeezed states [26] for noise reduction etc. The periodic orbit makes two circles to close up again (figure two in row two) in Fig. 4 (on the right). The Poincaré map has two points in each period T and there is a new peak at $\omega/2$ in the power

spectrum (the rightmost figure in row two) in Fig. 4. The current on the right has new oscillations with half the original frequency and all their superharmonics. This subharmonic signal can then be used in various ways: To produce a signal of half the original frequency. To compress the signal into a desirable frequency range or to squeeze out of it undesirable noise. The signatures of this bifurcation are: An additional oscillation in the current. An extra loop in the periodic orbit on phase portrait. Two points replacing one in the Poincaré map. Half the fundamental frequency and its superharmonics in the power spectrum.

The Chaotic Attractor and Random Sequences: The period doubling of the periodic orbit continues into a period-doubling cascade to a strange attractor. We will use this attractor to generate ultrafast random sequences at room temperatures. This is very important to do for secure data storage and transmission [23, 40, 45], stochastic modeling [4], and Monte Carlo simulations [10]. So far the fastest available technology for this task have been semiconductor lasers. We plan to find the parameter regions where the chaotic attractors exist and where their detection can be optimized. This parameter region my be enlarged by the addition of noise, as in [1], and we will explore different types noise and its effect on the simulations. The signatures of the strange attractors are: A wide range of oscillations in the current. A strange attractor in phase portrait. A complex Poincaré map. Broadband noise in the power spectrum.

The Torus (Mixer) and a Distinct Chaotic Attractor: It is still not clear whether a second Hopf bifurcation producing a torus in the phase space is possible in the superlattices that have been designed so far [31]. This bifurcation occurs on row three in Fig. 4, for the quantum well. The bifurcation is generic but may be prohibited by the symmetries of the superlattice. We will try to design a superlattice for which the (even) symmetry is broken and the second Hopf bifurcation of the periodic orbit to a torus takes place. The orbits on the torus are quasi-periodic and are composed of two frequencies. This makes the torus a candidate for a frequency mixer with two tunable frequencies. Then we will explore the cascade of quasi-periodic orbits on this torus to a strange attractor, as the voltage bias increases. This strange attractor has different properties than the strange attractor created by the period-doubling cascade above and gives an alternative method to generate ultrafast random sequences at room temperatures. We plan to compare the sequences generated by the two types of attractors and see if one has some advantage over the other. We also will find the parameter regions where these latter types of chaotic attractors exist and where their detection can be optimized. This parameter region my be enlarged by the addition of noise as above, and we will explore different types noise and its effect on the simulations.

However, we also see that there are only two occupies states below the Fermi levels (hill) on Fig. 6. This is analogous to the situation of Galdrikian and Birnir [25] and distinct from that of Batista et al. [6]. In the latter case there are three occupied states below the Fermi level. In fact, three states are necessary for the second Hopf bifurcation above and the cascade of quasi-periodic orbit the strange attractor. Thus

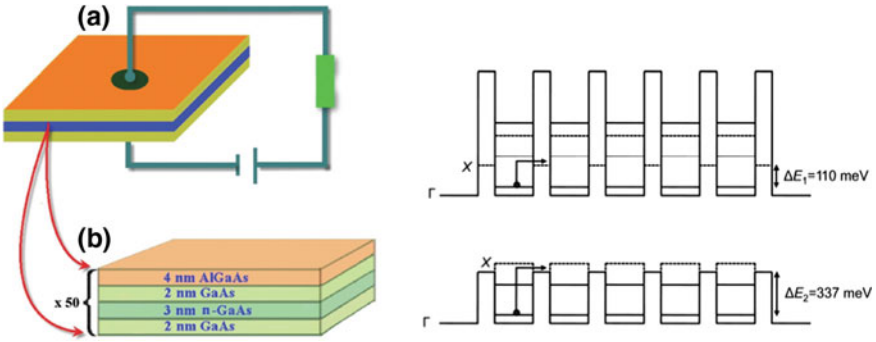

Fig. 6 Left: schematic diagram of a dc voltage-biased SSL, from Bonilla et al. [12]. Right: The band diagram of a GaAs/$Al_{0.7}Ga_{0.3}As$ SSL (**a**) and GaAs/$Al_{0.45}Ga_{0.55}As$ SSL (**b**), from Huang et al. [37]. The conduction band and the bound states of the wells are indicated by the solid horizontal lines. The bottom of the X-valley is indicated by the dashed lines

we need to redesign the SL to enable the bifurcation to the torus above and the resulting quasi-periodic orbits. We also have to make sure that the even symmetry of the SL is broken, so the signal is stronger and easier to observe.

10 Semiconductor Superlattices

The observation of Bloch oscillations in semiconductor superlattices (SSLs) [36] has led to many proposed applications of these heterostructures as sources and detectors at gigahertz and terahertz frequencies. More recently, nonlinear Gunn oscillations and chaotic dynamics have been observed in SSLs in the sequential tunneling regime. These nonlinear phenomena present the opportunity for development of new applications of SSLs, such as true random number generators and frequency mixers. Furthermore, recent advances in the design of SSLs have opened the possibility of realizing these applications at room temperature. In support of the development of applications of SSLs in the nonlinear regime, we theoretically characterize the nonlinear dynamical phenomena of the sequential resonant tunneling (SRT) model of weakly-coupled SSLs in this paper. We show the effects on the bifurcation diagram from variations of the number of periods making up superlattice, the sensitivity of the SRT model to time-dependent stochastic fluctuations in the bias voltage and local tunneling rates, and the effect of time-independent random perturbations of the widths of the wells and barriers. This and the next three sections follow [21].

Spontaneous oscillations, quasiperiodic orbits, and chaos have already been observed experimentally at very low temperatures [34, 36, 47] and at room temperature [31–33, 37, 41] in 50-period SSLs with noisy voltage sources. Simulations by Alvaro et al. [1] exhibited a strong chaotic signal. Experiments by Huang et al. [31, 32] show that heating suppresses the nonlinear phenomena in SSLs, and we

suspect this also occurs in single QWs. Huang et al. also describe a way of suppressing the effect of heating, enhancing the current oscillations: It was hypothesized that at warm temperatures, phonon-assisted transport though the X-valley of AlAs allowed a thermal distribution of carriers to diffuse through the SSL, overwhelming the nonlinear quantum dynamics. This effect was suppressed by choosing the Aluminum concentration of GaAs/AlGaAs wells in order to maximize the lowest bandgap energy, i.e. make the X and Γ band gaps equal to one another (Fig. 6). As a result, current oscillations were observed in SSLs at room temperature for the first time, see [31, 32].

We consider the SRT theory of Bonilla et al., which describes the electronic dynamics of SSLs in the weakly-coupled, self-consistent regime [15]. Two different time scales are taken into account in this description of SSLs. The inter-site tunneling and inter-subband relaxation processes occur on much shorter timescales than the dielectric relaxation processes [12]. Therefore, the long timescale dynamics of semiconductor lasers [44] and superlattices [1, 14] are typically modeled using semiclassical equations, while the short timescale processes are treated separately as noise. In the case of the SRT model, the short-timescale processes are included through the addition of stochastic terms to the dynamical equations. Nonlinearities enter the model via the inter-site Coulomb interaction, which bends the conduction band of the SSL, modifying the inter-band tunneling rates by casting the energy levels of adjacent wells into or out of resonance [12]. The dynamical equations are discussed in detail in Sect. 11. The bias voltage, V_{bias}, is treated as an external parameter of the model. Gunn-like oscillations in $J(t)$ are found to occur in the SRT model over several intervals of V_{bias} [16, 20]. These oscillations undergo a series of bifurcations, which may cascade into chaotic behavior [1]. In [42], we characterized the route to chaos via analysis of the Poincaré map and power spectrum, and distinguished the effects of the noise terms from the deterministic chaos.

For sufficiently small bias voltages, the total current $J(t)$ through the SSL responds linearly to changes in the bias voltage. At higher bias voltages, $J(t)$ suddenly transitions to a time-dependent, oscillatory function, which passes through a further series of transitions leading to chaotic behavior. We summarize the behavior of $J(t)$ below:
Fixed-point: Over certain voltage intervals, $J(t)$ is attracted toward a stationary value.
Bistability: The first signal of the nonlinear dynamics is a bistable response of $J(t)$ to slow variations in V_{bias}. This behavior is observable only at sufficiently low temperatures [16, 20]. Generically, bistable behavior is found at voltages near the Hopf bifurcation described below.
Supercritical Hopf Bifurcation: As the bias voltage is increased, we next observe a supercritical Hopf bifurcation. The fixed point becomes unstable, and $J(t)$ evolves to a periodic orbit. The periodic orbit is topologically equivalent to a circle in phase space, which corresponds to a one-cycle of the Poincaré map. In this regime, the SSL acts as a GHz oscillator with a discrete power spectrum involving the frequencies $f_n = n/T$, $n = 1, 2, 3, \ldots$, where T is the period of the lowest-frequency oscillation present. The superharmonics $n > 1$ arise due to the nonlinearities present in the SRT model. In this dynamical phase, the fundamental period T varies smoothly with the bias voltage, therefore the oscillator is also *tunable*. By filtering out all but the desired

harmonic and fine-tuning it via the bias voltage, a wide range of frequences may be selected.

Period Doubling Bifurcation: In this regime, one-cycles of the Poincaré map transition to two-cycles. The fundamental period of the oscillator is doubled, $T \to 2T$, and the fundamental frequency is cut in half: $\omega \to \omega/2$. A new frequency peak will appear in the spectrum at half the fundamental frequency, and the number of superharmonics will double. Following a period doubling bifurcation, the reverse (period-halving) bifurcation may occur. We refer to the regions between these bifurcations as *period doubling bubbles*. An application of period doubling, due to the subharmonic peak, is that a signal may be read at lower frequency, where the noise may be reduced, and it can be used to make squeezed states [26].

Period Doubling Cascade: Period doublings may occur in succession over certain voltage intervals, and an infinite number of doublings is possible in a finite voltage range. The invariant phase space structures transition from compact manifolds (periodic orbits of high periods) to chaotic attractors. The Poincaré map takes on a fractal structure. Our simulations show that the SRT model does not support true quasiperiodic orbits, hence the chaotic attractor is the most complex structure in the bifurcation diagram. It is the result of a cascade of a period doubling sequence of periodic orbits. An application of the chaotic dynamics in this regime is ultrafast generation of random number sequences [37]. This has many applications in areas such as secure communication and data storage, stochastic modeling, and Monte Carlo simulations, see [4, 23, 40, 45]. Previously the generation of ultrafast random number sequences has been accomplished by fast semiconductor lasers but these require a mixture of optical and electronic components. SSLs on the other hand are entirely submicron devices that can be readily integrated into complex circuits.

In previous theoretical studies of optically-driven quantum wells, it was discovered that the introduction of one or more off-center "steps" in the confinement potential, see Fig. 7, had a profound impact on the character of the nonlinear phenomena. In the presence of a single step, a period-doubling bifurcation in the electronic response was predicted to occur near the intersubband resonant frequency at high doping densities and strong driving fields. The presence of a second step unfolded the period-doubling bifurcation into a supercritical Hopf bifurcation which gener-

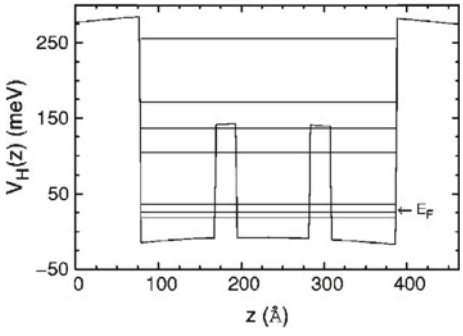

Fig. 7 The stationary self-consistent potential resulting from the band structure and Coulomb potential of the asymetric GaAs/AlGaAs quantum well, taken from Batista et al. [5]. The energy levels of the bound states are indicated by the horizontal lines

ated quasiperiodic behavior. Both single- and double-stepped assymetric quantum wells also exhibited period-doubling cascades to chaos. In analogy with these results, we consider the possibility of unfolding the period doubling bifurcation of the SRT model into a Hopf bifurcation, by breaking the periodic symmetry of the SSL, which we term "disordered superlattice."

11 Model

Many phenomena are captured by means of a quasi-one-dimensional resonant sequential tunneling model of nonlinear charge transport in SSLs [13–15]. Consider a weakly coupled superlattice having N identical periods of length l and total length $L = Nl$ subject to a dc bias voltage V_{bias}. The evolution of F_i, the average electric field at the SSL period i, and the total current density, $J(t)$, is described by Ampere's law

$$J(t) = \epsilon \frac{dF_i}{dt} + J_{i\to i+1}, \tag{6}$$

and the voltage bias condition

$$\sum_{i=1}^{N} F_i = \frac{V_{\text{bias}}}{l}. \tag{7}$$

Fluctuations of F_i away from its average value $F_{\text{avg}} = eV_{\text{bias}}/L$ arise from the intersite tunneling current $J_{i\to i+1}$, which appears in Eq. (6). A microscopic derivation of $J_{i\to i+1}$ produces the result [12, 13]

$$J_{i\to i+1} = \frac{en_i}{l} v^{(f)}(F_i) - J^{-}_{i\to i+1}(F_i, n_{i+1}, T), \tag{8}$$

in which n_i is the electron sheet density at site i, $-e < 0$ is the electron charge and T is the lattice temperature. Here the forward velocity, $v^{(f)}(F_i)$, modeled as a Lorentzian distribution, is peaked at resonant values of F_i for which one or more energy levels at site i are aligned with the levels at site $i + 1$. The backward tunneling current is given by

$$J^{-}_{i\to i+1}(F_i, n_{i+1}, T) = \frac{em^* k_B T}{\pi\hbar^2 l} v^{(f)}(F_i) \ln\left[1 + e^{-\frac{eF_i l}{k_B T}}\left(e^{\frac{\pi\hbar^2 n_{i+1}}{m^* k_B T}} - 1\right)\right], \tag{9}$$

where the reference value of the effective electron mass in $Al_xGa_{1-x}As$ is $m^* = (0.063 + 0.083x)m_e$, and k_B is the Boltzmann constant. The n_i are determined self-consistently from the discrete Poisson equation,

Table 1 (Top) The design parameters of the superlattice. (Bottom) Values of the potential barrier and energy levels for GaAs/$Al_{0.7}Ga_{0.3}As$ and GaAs/$Al_{0.45}Ga_{0.55}As$ superlattices, first and second row, respectively

T (K)	N_D (cm^{-2})	d (nm)	w (nm)	s (μm)
295	6×10^{10}	4	7	60
V_{barr} (meV)	E_1 (meV)	E_2 (meV)	E_3 (meV)	
600	53	207	440	
388	45	173	346	

$$n_i = N_D + \frac{\epsilon}{e}(F_i - F_{i-1}), \tag{10}$$

where N_D is the doping sheet density and ϵ is the average permittivity. The field variables F_i are constrained by boundary conditions at $i = 0$ and $i = N$ that represent Ohmic contacts with the electrical leads

$$J_{0\to 1} = \sigma_0 F_0, \quad J_{N\to N+1} = \sigma_0 \frac{n_N}{N_D} F_N, \tag{11}$$

where σ_0 is the contact conductivity. Shot and thermal noise can be added as indicated in [1, 17].

Table 1 gives the numerical values of the parameters used in the simulations. The GaAs/$Al_{0.45}Ga_{0.55}As$ configuration corresponds with the configuration used in experiments [31, 37, 48]. The rest of the parameters are as follows: $A = s^2$ is the transversal area of the superlattice, d and w are the barrier and well lengths, and $l = d + w$ is the SSL period. The contact conductivity is a linear approximation of the behavior of $J_{0\to 1}$, which depends on the structure of the emitter; the value has been taken to reproduce the experimental results produced by Huang et al. with $N = 50$: $\sigma_0 = 0.783$ A/Vm for $V_{barr} = 388$ meV ($x = 0.45$) and $\sigma_0 = 0.06$ A/Vm for $V_{barr} = 600$ meV ($x = 0.7$), where V_{barr} is the height of the barrier [1, 31].

11.1 Noise

To model the unavoidable fluctuations in the bias voltage, as well as the short-timescale processes in the electronic dynamics, stochastic terms are introduced into evolution equations [1]. To account for the noise in the bias voltage, Eq. (7) is modified to

$$\sum_{i=1}^{N} F_i = \frac{V_{\text{bias}} + \eta(t)}{l}, \tag{12}$$

where $\eta(t)$ is taken to be a Gaussian random variable with standard deviation σ_η. To account for the short-timescale processes at each site of the SSL, Eq. (6) is modified to include fluctuations in the tunneling current

$$\varepsilon \frac{dF_i}{dt} + J_{i\to i+1}(F_i) + \xi_i(t) = J(t), \tag{13}$$

where

$$\langle \xi_i(t)\xi_j(t')\rangle = \frac{e}{A}\left[\frac{ev^{(f)}(F_i)}{l} n_i + J^{-}_{i\to i+1}(F_i, n_{i+1}, T) + 2J^{-}_{i\to i+1}(F_i, n_i, T)\right]\delta_{ij}\delta(t-t'). \tag{14}$$

We may observe that $\eta(t)$ is independent of i, while $\xi_i(t)$ are independent Gaussian random variables associated with each site of the SSL. The strength of the fluctuations in the bias voltage may be tuned via the empirical parameter σ_η, while the strength of the fluctuations in the local tunneling current is completely determined by the other parameters, see Table 1.

11.2 Disorder

We also consider time-independent perturbations that break the periodic symmetry of the superlattice. We introduce variations in the widths of the wells and barriers via the scaling parameters β_i and ζ_i. The perturbed well and barrier lengths are

$$w_i = \beta_i w \tag{15}$$

$$d_i = \zeta_i d. \tag{16}$$

Both β_i and ζ_i are taken to be uncorrelated, normally-distributed random numbers with standard deviation σ. We constrain the total length of the SL to preserve the validity of the bias equation, (7), by forcing the condition that $\sum_i \beta_i = \sum_i \zeta_i = N$. To lowest order, the energy levels scale with β_i according to

$$\varepsilon_i^{C,m} = \frac{\varepsilon^{C,m}}{\beta_i^2}. \tag{17}$$

These modifications imply that the effective dielectric constant becomes dependent on i,

$$\varepsilon_i = l_i/(w_i/\varepsilon_w + d_i/\varepsilon_d). \tag{18}$$

Equation (7) becomes

$$V_{\text{bias}} = \sum_{i=1}^{N} F_i l_i. \tag{19}$$

Following Bonilla et al. [16], Eqs. (8) and (9) are modified to account for the effects of disorder on $v^{(f)}(F_i)$ and τ_i:

$$v^{(f)}(F_i) = \frac{\hbar^3}{2m^{*2}} \sum_{m=1}^{3} \frac{l_i\left(\gamma_{C,1} + \gamma_{C,m}\right)\tau_i(\varepsilon^i_{C,m})}{\left(\varepsilon_i^{C,1} - \varepsilon_{i+1}^{C,m} + eF_i\left(d_i + \frac{w_i + w_{i+1}}{2}\right)\right)^2 + \left(\gamma_{C,1} + \gamma_{C,m}\right)^2} \tag{20}$$

$$\tau_i = \frac{16k_i^2 k_{i+1}^2 \alpha_i^2}{\left(k_i^2 + \alpha_i^2\right)\left(k_{i+1}^2 + \alpha_i^2\right)\left(w_i + \frac{1}{\alpha_{i-1}} + \frac{1}{\alpha_i}\right)\left(w_i + \frac{1}{\alpha_{i+1}} + \frac{1}{\alpha_i}\right)e^{2\alpha_i d_i}} \tag{21}$$

where

$$\hbar k_i^m = \sqrt{2m^* \varepsilon_i^{C,m}} \tag{22}$$

$$\hbar k_{i+1}^m = \sqrt{2m^*\left(\varepsilon_i^{C,m} + e\left[d_i + \frac{1}{2}\left(w_i + w_{i+1}\right)\right]F_i\right)} \tag{23}$$

and

$$\hbar \alpha_{i-1}^m = \sqrt{2m^*\left(eV_b + e\left[d_{i-1} + \frac{w_i}{2}\right]F_i - \varepsilon_i^{C,m}\right)} \tag{24}$$

$$\hbar \alpha_i^m = \sqrt{2m^*\left(eV_b - e\left[\frac{1}{2}w_i\right]F_i - \varepsilon_i^{C,m}\right)} \tag{25}$$

$$\hbar \alpha_{i+1}^m = \sqrt{2m^*\left(eV_b - e\left[d_i + \frac{1}{2}w_i + w_{i+1}\right]F_i - \varepsilon_i^{C,m}\right)} \tag{26}$$

12 Numerical Methods

The evolution Eqs. (6)–(11) are evolved in time using the forward Euler method and the trajectory $(F_i(t), n_i(t), J(t))$ through the $(2N + 1)$-dimensional phase space is stored. When applicable, the stochastic terms ($\xi_i(t)$ and $\eta(t)$) are included using the Euler-Maruyama method. We utilize the standard methodology of dynamical systems theory (analysis of the Poincaré map) in order to characterize the dynamical phenomena of the SRT model: The first step is to construct the phase portrait, i.e. to project the evolution onto a two-dimensional surface in phase space. We choose the surface spanned by the the coordinates (F_i, F_j) for some values of i and j near the anode and cathode respectively of the SSL.

The next step is to compute the Poincaré map of the phase portrait. After sufficient time has elapsed, and regardless of the initial conditions, the phase space trajectory settles onto one of the following time-invariant structures: (a) Fixed point, (b) periodic orbit, (c) strange attractor. The Poincaré map is used in order to easily distinguish between these structures. It is computed according to the following pro-

cedure: First, the transient behavior associated with the initial conditions is excised from the trajectory and only the remaining data is considered in what follows. When $F_i(t)$ passes through its central value, the time t^* and the field $F_j(t^*)$ are stored. We also compute the quantity $\dot{F}_i(t^*)$ from Eq. (6). We then discard all of the values of t^* for which $\dot{F}_i(t^*) > 0$, in order to prevent sampling the same orbit more than once per cycle. The Poincaré map transforms the essentially continuous trajectory through phase space into a discrete map from the one-dimensional interval onto itself [18]. We represent it visually in one of two ways: Either (a) phase portraits, plotting $F_j(t^*)$ against $\dot{F}_j(t^*)$, c.f. Fig. 9, or (b) bifurcation diagrams, plotting $F_j(t^*)$ against some external parameter such as the bias voltage, c.f. Fig. 8.

Both fixed points and periodic orbits appear as a single point in the visualization of the Poincaré map. However, fixed points are easily distinguished from periodic orbits (one-cycles) by computing the power spectrum associated with the current $J(t)$:

$$P[J](f) = \left| \int_{t_i}^{t_f} dt\, e^{-i2\pi f t} J(t) \right|^2 , \tag{27}$$

where f is the frequency. A period-doubling bifurcation is identified when one-cycles transition to two-cycles, producing two points in the Poincaré map. Chaotic regions are identified where a proliferation of period-doubling bifurcations occur, and the number of points in the Poincaré map increases without bound, yielding a fractal structure in the bifurcation diagram.

Dynamical structures revealed by the Poincaré map are associated with various power spectra as follows: (a) periodic orbits correspond to a series of peaks with widths of the same order as the frequency bin size, falling at integer multiples of the fundamental frequency, (b) period doubling bifurcations are recognized when the number of peaks in the spectrum changes by a factor of two, and a new peak appears in the power spectrum at half the fundamental frequency, (c) chaotic attractors exhibit power spectra containing both sharp peaks and broadband noise.

The boundary conditions are more subtle that indicated in Sect. 3 in the THz regime or Sect. 11 in the GHz regime. The leads should be treated as a semiclassical system that we are coupling with (highly) quantum system, namely the superlattice. This coupling involves a very large number of states and is best treated numerically. For an effective treatment using perfectly matched layers (PML), see Chaps. 2 and 3 in [22].

13 Results

We simulate superlattices and characterize the dynamical instabilities that may be applied to create sources, period halvers and squeezers, random sequence generators and frequency mixers, even at room temperature. The dynamical equations (6)–(11)

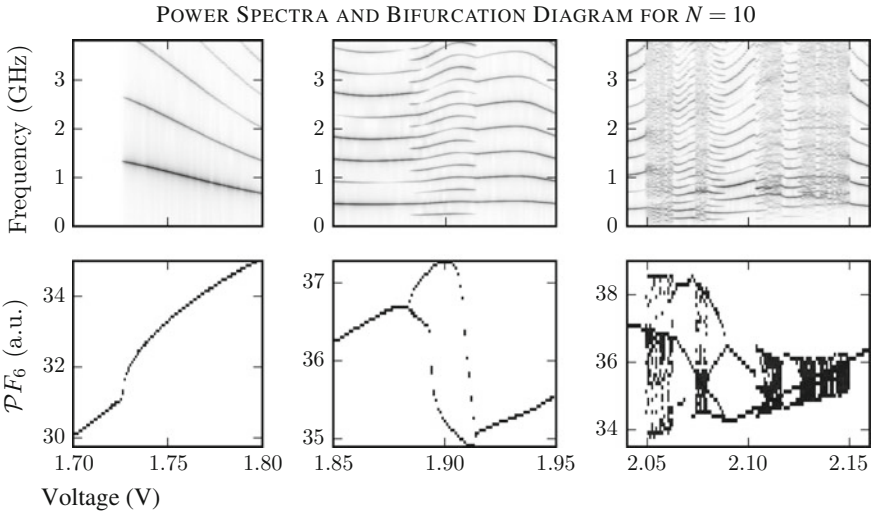

Fig. 8 (Top row) The power spectrum of $J(t)$ plotted against the bias voltage, taken from [42]. (Bottom row) The bifurcation diagram, plotting the Poincaré map against the bias voltage. The Hopf bifurcation from the steady state is shown in the first column. A period doubling "bubble" is shown in the second column. A period-doubling cascade is shown in the third column

are evolved using the parameter values listed in Table 1 for a GaAs/$Al_{0.7}Ga_{0.3}$As SSL, with the quantized energy levels corresponding to $V_{barr} = 600$ meV. The GaAs/$Al_{0.7}Ga_{0.3}$As SSL is treated here in order to illustrate bifurcations as clearly as possible, but the same phenomena and instabilities occur in $Al_{0.45}Ga_{0.55}$As SSLs [21]. Dynamical instabilities are found in two distinct *plateaus*, over which which the local electric fields of the SSL cease to increase monotonically as a function of V_{bias}. The *first plateau* occurs at very low voltages, with tunneling transport between the ground states of adjacent wells that are nearly aligned with one another in energy. The *second plateau* occurs in the region of V_{bias} where the the electric fields bend the potential of the SSL to align the ground state of well i with first excited state of well $i + 1$. We do not observe a third plateau because the third excited state becomes unbound at bias voltages that align it with the first excited state of an adjacent well.

The leading edge, i.e. the lowest value of V_{bias} contained in a plateau, is identified by a supercritical Hopf bifurcation from fixed point to periodic orbit, as shown the leftmost column of Fig. 8. At low temperatures, the Hopf bifurcation may be preceded by bistability, but at higher temperatures this phenomenon is suppressed. Within a plateau, we may observe period-doubling, period-doubling cascades, and chaotic attractors whose locations depend upon on the values of the rest of the parameters, in particular N, the number of wells making up the superlattice. As a general rule, shorter superlattices exhibit a greater variety of dynamical behavior in the second plateau. In SSLs ($N \leq 10$), the Hopf bifurcation in the first plateau disappears and the first plateau is not present. As N increases, the dynamical instabilities appear to move

from the second plateau into the first plateau: Near $N = 20$, the Hopf bifurcation appears in the first plateau. In longer SSLs ($N \geq 30$), the second plateau contains only a supercritical Hopf bifurcation to a periodic orbit without any further bifurcations, while the first plateau has gained a period-doubling bubble. In this section, we give a detailed description of the dynamical instabilities of $N = 10$ SSLs, then we point out the effect of increasing N. We close with a discussion of the effects of stochastic terms and disorder on the dynamical instabilities.

13.1 N=10

As mentioned above, the first plateau does not exist for $N = 10$, and all oscillatory behavior takes place in the second plateau. Combining the bifurcation diagram, power spectra and phase portraits shown in Figs. 8 and 9, we characterize the dynamical instabilities of the SRT model for $N = 10$:

Supercritical Hopf Bifurcation: In the leftmost column of Fig. 8, we observe a transition from a stationary state to a periodic orbit. Subsequently, we observe a circle in the phase portrait, similar to the top row of Fig. 9. The Poincaré map consists of a single point, or one-cycle, when visualized. The power spectrum contains peaks falling at integer multiples of a fundamental oscillation frequency as demonstrated in the top row of Fig. 8. In this regime, the SSL acts as a GHz oscillator with a discrete power spectrum involving the frequencies $f_n = n/T,\ n = 1, 2, 3, \ldots$, where T is the period of the lowest-frequency oscillation. The superharmonics $n > 1$ arise due to nonlinearities of the SRT model. We also observe that the fundamental frequency and resulting superharmonics can be continuously tuned by variation of V_{bias} as demonstrated in Fig. 8.

Period Doubling Bifurcation: A period-doubling bifurcation is identified by a doubling of the orbits in phase space and consequent doubling of the number of points in the Poincaré map. We illustrate this phenomena in the transition between rows one and two of Fig. 8 and in the second row of Fig. 9. The power spectrum gains a *subharmonic* peak at half of the former fundamental frequency, and consequently we observe twice as many superharmonics in the power spectrum. A period-doubling bifurcation may be followed by a period-halving bifurcation forming a period-doubling bubble as shown in the second column of Fig. 8.

Period Doubling Cascade: A period doubling cascade is identified when many period-doubling bifurcations occur in rapid succession over some interval of the bias voltage. In principle, an infinite number of doublings may occur over a finite voltage interval. This process terminates when the phase space orbits lose their periodicity altogether and the Poincaré map takes on the characteristics of a chaotic attractor. An example of a period-doubling cascade is illustrated in the last three rows of Fig. 9. The rightmost column of Fig. 8 also shows several period-doubling cascades

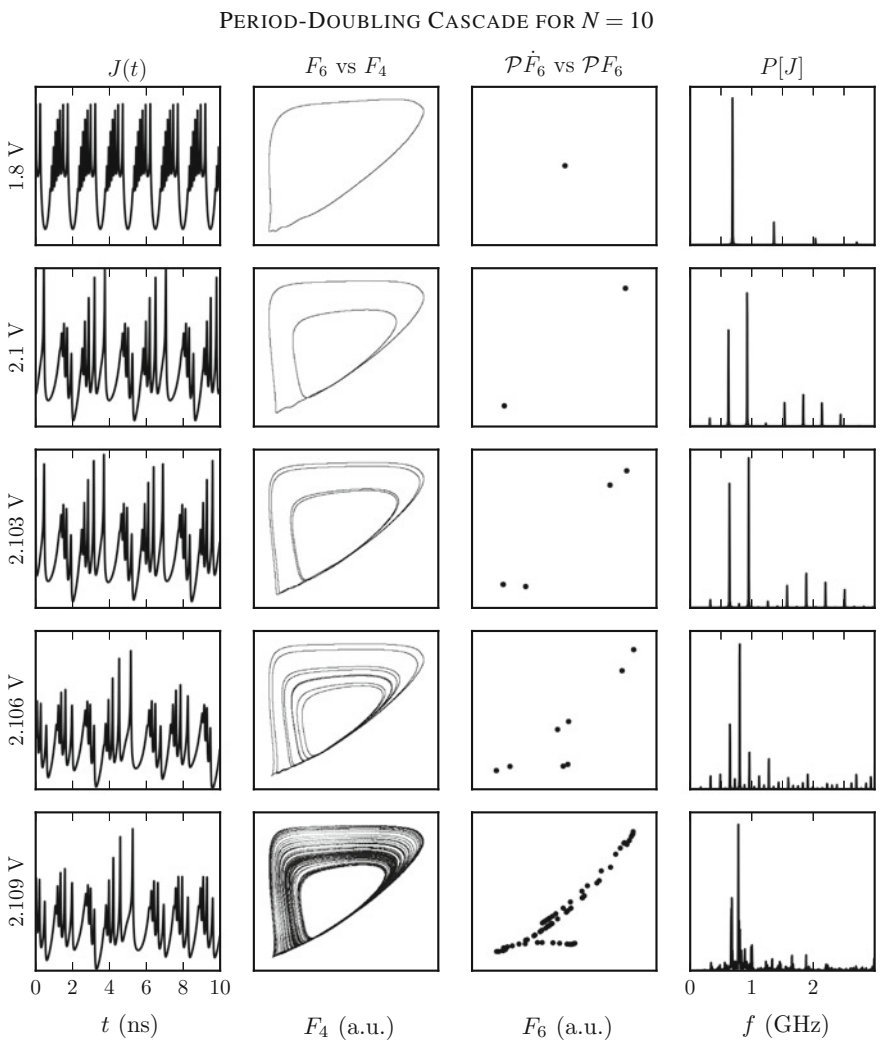

Fig. 9 Representative phase portraits, taken from [42]. The first column shows the average current J plotted against time t. The second column shows the phase portrait $F_6(t)$ plotted against $F_4(t)$. The third column shows the Poincaré map $\mathscr{P}\dot{F}_6(t^*)$ plotted against $\mathscr{P}F_6(t^*)$. The last column shows the power spectrum of $J(t)$. A periodic oscillation is shown in the first row. A period-doubling bifurcation is observed in the second row. The period-doubling cascade to a chaotic attractor is shown in the bottom four rows

connected by regions of orbits with very high periods. The broadening and merging of peaks in the power spectrum is characteristic of a chaotic attractor. We also compute the Feigenbaum constant of the cascade near 2.109 V, shown in Figs. 8 and 9. We introduce the formula

$$\delta_n = \frac{V_{n-1} - V_{n-2}}{V_n - V_{n-1}}, \tag{28}$$

where V_n are the voltages corresponding to the nth doubling in the cascade. For a period-doubling cascade, $\delta_n \to 4.6692\ldots$ as $n \to \infty$. By taking sufficiently small steps (about 10^{-6} V) in the parameter V_{bias}, we have measured the first Feigenbaum constant with less than 1% error. We conclude that the route to chaos in the SRT model is a period-doubling cascade.

13.2 N > 10

We next describe the effects of increasing number of periods making up the SSL, keeping all other parameters fixed. In the case of $N = 20$, both the first and second plateaus are present. The supercritical Hopf bifurcation corresponding to the beginning of the first plateau is shown in the first column of Fig. 10. No other bifurcations are observed in the first plateau. The onset of the second plateau is shown in the second column of Fig. 10. In the second plateau, we again find period doubling cascades to chaotic attractors; this behavior is illustrated in the third column of Fig. 10. Comparing the third columns of Figs. 8 and 10, we observe that the period-doubling cascade and the chaotic attractor occur over narrower voltage intervals in the $N = 20$ case compared with the $N = 10$ case. For higher values of N, the voltage intervals containing the period doubling bifurcations become increasingly narrow, and eventually disappear entirely from the second plateau near $N = 30$.

As N is increased, we observe the appearance of more dynamical instabilities in the first plateau. A period-doubling bubble emerges in the first plateau near $N = 25$ and subsequently widens over a larger interval of V_{bias} with increasing N. This bubble is responsible for the period-two orbit illustrated in the top panel of Fig. 12 for the case of $N = 50$. There are no further period-doubling bifurcations present in the first plateau for this value of N. For $N = 100$, simulations by Amann *et al.* showed chaotic dynamics occur in the first plateau [2]. This result fits with the trend of dynamical instabilities moving from the second plateau to the first plateau as N increases.

13.3 Noise

We next consider the effects of the stochastic terms in Eqs. (12) and (13), which model the effects of a noisy voltage source and intrinsically random tunneling processes. We observe that the dynamics become increasingly sensitive to noise with increasing

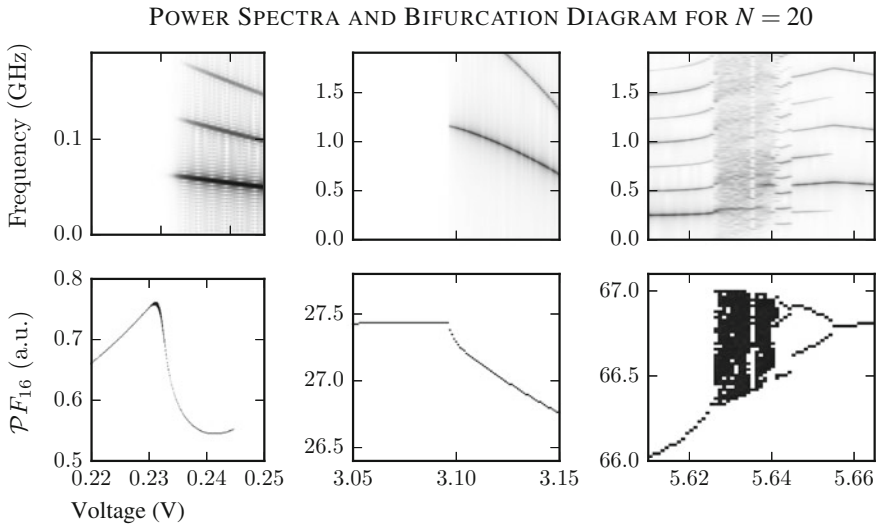

Fig. 10 (Top row) The power spectrum of $J(t)$ plotted against the bias voltage. (Bottom row) The bifurcation diagram, plotting the Poincaré map against the bias voltage. The Hopf bifurcation from the steady state in the first plateau is shown in the first column. The Hopf bifurcation from the steady state in the second plateau is shown in the second column. A narrow region in the second plateau containing a chaotic attractor is shown in the third column

N. For the case of $N = 10$, regions of interest in the bifurcation diagram are plotted in Fig. 11. We have chosen these voltage intervals to be the same as in Fig. 8 for clear comparison. We observe that the addition of noise stimulates the Hopf bifurcation to occur at lower voltages, which widens the second plateau. Noise also has the effect of broadening the peaks in the power spectrum as shown in the first row of Fig. 11.

Upon perturbation by noise, period-doubling behavior may be enhanced and higher period orbits may occur over a particular window of V_{bias} than do in the noise-free case, see Fig. 12. demonstrates the effect of very small perturbations by noise on the phase portrait over the window containing the period-doubling bubble, which occurs in the first plateau for the $N = 50$ case. For higher-period orbits, the broadening effect of perturbations on the power spectrum can cause the narrowly spaced peaks in the spectrum to merge, transforming high-period orbits to chaotic attractors as demonstrated in Fig. 11. This effect may broaden the windows in which chaotic attractors occur, connecting chaotic attractors that are distinct in the noise-free limit as demonstrated by comparison of the chaotic regions in Figs. 8 and 11.

Periodic orbits in the first plateau for $N = 50$ are more sensitive to noise than those which occur in the second plateau for $N = 10$. This difference is evident upon comparison of Fig. 11 with Fig. 12, in particular the power spectra. We see similar results but have used much less noise to produce Fig. 12 than Fig. 11. The bottom panel of Fig. 12 shows that the inclusion of noise terms may cause the Poincaré map and power spectrum to resemble those of a chaotic system. However, we simulate

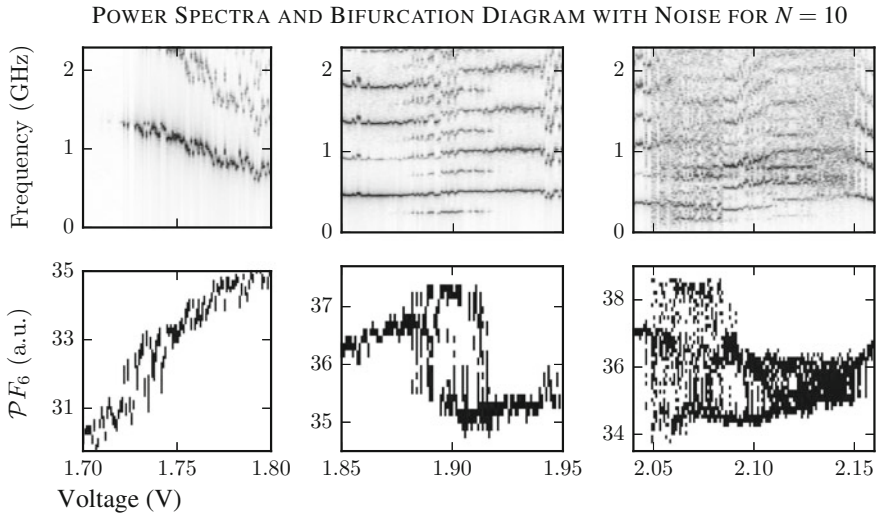

Fig. 11 (Top row) The power spectrum of $J(t)$ plotted against the bias voltage. (Bottom row) The bifurcation diagram, plotting the Poincaré map against the bias voltage. The Hopf bifurcation from the steady state is shown in the first column. A period doubling bubble is shown in the second column. A period-doubling cascade is shown in the third column. $\sigma_\eta = 1.4 \times 10^{-5}$ V

the same situation in the absence of noise in the top panel of Fig. 12. While the SRT model is very sensitive to noise in this regime, the underlying dynamical structure is an orbit of period two, and hence our numerical methods are able discern between noise-sensitivity and true dynamical chaos.

13.4 Disorder

Sensitivity to disorder is independent of N. The model is more sensitive to disorder with correlations between β_i and ζ_i. The introduction of noise decreases the effect of disorder.

The values of V_{bias} at which a particular instability (Hopf bifurcations, period-doublings, period-doubling cascades, and chaotic attractors) occurred in our simulations was shifted upon the introduction of disorder, broadening the voltage windows where it is *possible* for a certain bifurcation to occur. This means that the introduction of disorder makes it possible for chaotic behavior to occur at lower *and* higher values of voltage bias, even for the same value of disorder. Figure 13 shows a chaotic attractor which is centered about the same value of V_{bias} but is much wider in the disordered SSL.

For sufficient values of σ, additional instabilities—including chaotic attractors, may occur which are not observed in the clean (free of disorder) case. Alternatively,

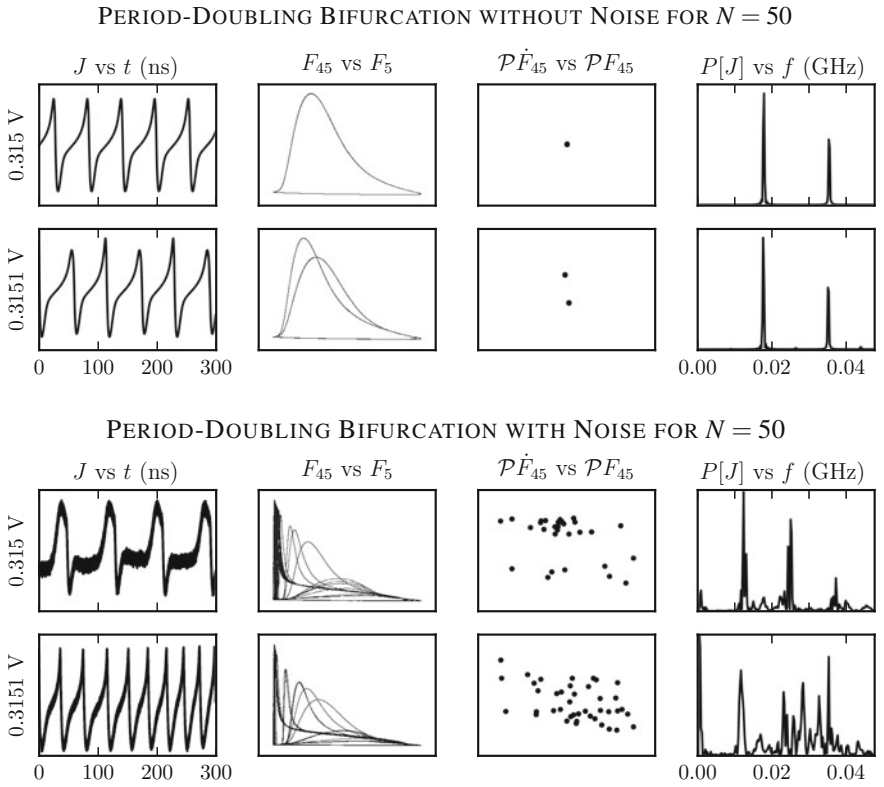

Fig. 12 Period doubling with and without noise. $\sigma_\eta = 2.8 \times 10^{-6}$ V

period doubling bifurcations that are present in the clean case may suppressed by the introduction of disorder, as demonstrated in Fig. 13.

Distinct chaotic attractors which occur in the second plateau for $N = 10$ are robust against disorder to varying degrees, and some have been observed to persist for large values of σ. Over multiple simulations, we have observed that the chaotic region near 2.25 V is the most robust to disorder as demonstrated in Fig. 13.

The enhancement or suppression of chaotic behavior and the voltage regions over which this may occur is dictated by the random numbers β_i and ζ_i so we believe it will be possible to design a superlattice with specific variations in lengths of wells and barriers to enhance the robustness of chaotic attractors.

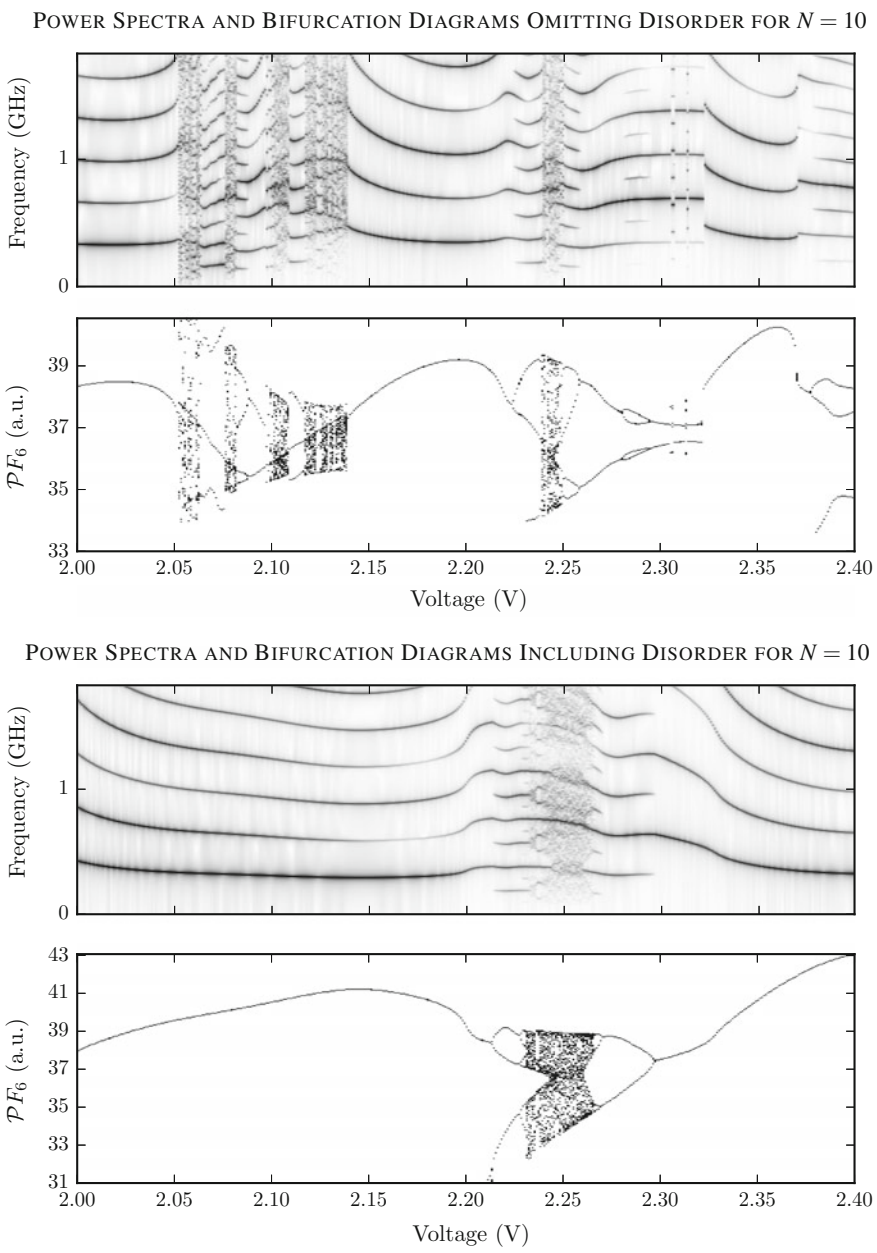

Fig. 13 (Top panel) Bifurcation diagram with $N = 10$ without disorder. (Bottom panel) Bifurcation diagram with disorder of strength $\sigma = 1\%$

14 Discussion

The connection that we are making between plasmon states in single quantum wells in the terahertz regime and density waves in superlattices in the gigahertz regime may seem to be a stretch. On the surface there are many differences between these systems. A superlattice of wells in the terahertz regime would be tightly coupled described by the equation in Sect. 3 with periodic boundary conditions, very different from the coupled equations in Sect. 11 describing the sequential tunneling model in the gigahertz regime. The boundary conditions are obviously different but in both cases we have a qualitative description for a range of parameters involved. The striking similarity between these two system is that their qualitative behavior is in both cases governed by coherent electron states. In the former case these are the plasmons slushing back and forth in quantum well. In the latter case they are the density waves executing Gunn oscillations in the superlattice. In both cases these oscillations exhibit bifurcations with increase in parameters. In the first case with increasing amplitude of the laser drive, in the second case the bifurcations take place with increased voltage bias. The bifurcating oscillations of the plasmons have been understood for a long time, but we have shown in [21, 42] that the density wave form a coherent electron state extending through the superlattice and the oscillations of these states show the same bifurcations at the same values of the bias throughout the lattice. This is observed by taking different Poincaré sections for different lattice site. They turn out to be qualitatively the same for all the lattice sites. Thus we see coherent electron states exhibiting generic bifurcations in both cases. Both of these systems are genuine nonlinear quantum systems of coherent electron states and this makes them qualitatively similar in spite of the physical differences.

15 Conclusions

We have shown that the nonlinear bifurcations found by simulations in single quantum wells in the terahertz regime [5, 6, 25] also occur in semiconductor superlattices (SSLs) in the gigahertz range [2, 3, 11]. The only exception is the second Hopf bifurcation to quasi-periodic orbits on a torus, but this can presumably also be accomplished with the design of more structure in SSL. The advantage of experiments on SSLs in the gigahertz range is that the experiments can be conducted at room temperature and indeed a chaotic oscillator due to the random dressing of a period two-orbit has already been measured [31, 32]. In [42] we have determined that the route to chaos for SSLs in the sequential tunneling regime is the period doubling cascade. Shorter (10-period) superlattices are observed to exhibit faster oscillations compared with longer (50-period) ones. Two plateaus are observed as functions of the voltage bias, and intrinsically chaotic dynamics on the second plateau are possible only for shorter SSLs, while the dynamics in the first plateau contain intrinsic chaos only for longer ($N > 50$) SSLs, see [21]. The robustness of these results to

stochastic perturbations in the local tunneling currents and the bias voltage was tested in [21]. It was observed that shorter SSLs are much less sensitive to noise compared with longer SSLs. Therefore two modes of random number generation are possible: Faster, intrinsic chaos in the second plateau for shorter superlattices, and slower, noise-enhanced chaos in the first plateau for longer superlattices, see [21] for more details.

The effects of random variations in doping density and the width of the wells and the barriers was also examined in [21]. It was found that the period-doubling cascade is robust to these perturbations, but the detailed shape of the bifurcation diagram can change significantly. Then these perturbations cannot unfold the period-doubling bifurcation into a second Hopf bifurcation as we initially conjectured. They are simply not strong enough to break the reflection symmetry of the constituent wells. To observe the second Hopf bifurcation it is essential that this symmetry is broken analogous to the work of Batista et al. [5, 6], then two or more states would also exist below the Fermi level. We conjecture this greater number of active states will be successful at exposing the second Hopf bifurcation in a properly designed SSL. It remains an open question whether all of these bifurcations can be extended to SSLs in the terahertz regime. This would signify a nontrivial technological progress since terahertz devices are difficult to make and operate at room temperature. It these bifurcations are found in teraherz range the possibility of making all the devices discussed above opens up and such devices can be operated at significantly faster time-scales.

Acknowledgements This material is based upon work supported by, or in part by, the U.S. Army Research Laboratory and the U. S. Army Research Office under contract/grant number 444045-22682.

References

1. M. Alvaro, M. Carretero, L. Bonilla, Noise-enhanced spontaneous chaos in semiconductor superlattices at room temperature. EPL (Europhys. Lett.) **107**, 37002 (2014)
2. A. Amann, J. Schlesner, A. Wacker, E. Schöll, Chaotic front dynamics in semiconductor superlattices. Phys. Rev. B **65**, 193313 (2002)
3. T. Ando, A.B. Fowler, F. Stern, Electronic properties of two-dimensional systems. Rev. Mod. Phys. **54**, 437 (1982)
4. S. Asmussen, P.W. Glynn. *Stochastic Simulation: Algorithms and Analysis*, vol. 57 (Springer Science & Business Media, 2007)
5. A.A. Batista, P.I. Tamborenea, B. Birnir, M. Sherwin, D.S. Citrin, Nonlinear dynamics in far-infrared driven quantum-well intersubband transitions. Phys. Rev. B **66**, 195325 (2002)
6. A.A. Batista, B. Birnir, P.I. Tamborenea, D.S. Citrin, Period-doubling and Hopf bifurcations in far-infrared driven quantum well intersubband transitions. Phys. Rev. B **68**, 035307 (2003)
7. B. Birnir, Chaotic perturbations of KdV equations: I. rational solutions. Phys. D Nonlinear Phenom. **18**, 464 (1986)
8. B. Birnir, R. Grauer, An explicit description of the global attractor of the damped and driven sine-Gordon equation. Commun. Math. Phys. **162**, 539 (1994)

9. B. Birnir, *Basic Attractors and Control* (To be published by Springer, New York, 2017)
10. K. Binder, D.W. Heermann, *Monte Carlo Simulation in Statistical Physics: An Introduction* (2002)
11. L.L. Bonilla, J. Galán, J. Cuesta, F.C. Martínez, J.M. Molera, Dynamics of electric field domains and oscillations of the photocurrent in a simple superlattice model. Phys. Rev. B **50**, 8644 (1994)
12. L.L. Bonilla, G. Platero, D. Sánchez, Microscopic derivation of transport coefficients and boundary conditions in discrete drift-diffusion models of weakly coupled superlattices. Phys. Rev. B **62**, 2786 (2000)
13. L.L. Bonilla, Theory of nonlinear charge transport, wave propagation and self-oscillations in semiconductor superlattices. J. Phys. Condens. Matter **14**, R341 (2002)
14. L.L. Bonilla, H.T. Grahn, Non-linear dynamics of semiconductor superlattices. Rep. Prog. Phys. **68**, 577 (2005)
15. L.L. Bonilla, S.W. Teitsworth, *Nonlinear Wave Methods for Charge Transport* (Wiley VCH, Weinheim, 2009)
16. L.L. Bonilla, R. Escobedo, G. Dell'Acqua, Voltage switching and domain relocation in semiconductor superlattices. Phys. Rev. B **73**, 115341 (2006)
17. L.L. Bonilla, M. Alvaro, M. Carretero, Chaos-based true random number generators. J. Math. Ind. **7**, 1 (2016)
18. P. Collet, J. Eckmann, *Iterated Maps on the Interval as Dynamical Systems*, Modern Birkhäuser Classics (Birkhäuser Boston, 2009)
19. K. Craig et al., Undressing a collective intersubband excitation in quantum well. Phys. Rev. Lett. **76**, 2382 (1996)
20. G. Dell'Acqua, L.L. Bonilla, R. Escobedo, Hopf Bifurcation in a Superlattice Model, in *Proceedings of the International Conference on Computational and Mathematical Methods in Science and Engineering* (2006)
21. J. Essen, M. Ruiz-Garcia, I. Jenkins, M. Carretero, L.L. Bonilla, B. Birnir, Parameter dependence of high-frequency nonlinear oscillations and intrinsic chaos in short GaAs/(Al,Ga)As superlattices (2017) (Submitted)
22. J. Essen, Simulations of open ballistic quantum systems and semiclassical semiconductor superlattices. Ph.D. thesis, University of California, Santa Barbara, 2017
23. R.G. Gallager, *Principles of Digital Communication* (Cambridge University Press, Cambridge, UK, 2008)
24. B. Galdrikian, M. Sherwin, B. Birnir, Self-consistent Floquet states for periodically driven quantum wells. Phys. Rev. B **49**, 13744 (1994)
25. B. Galdrikian, B. Birnir, Period Doubling and Strange Attractors in Quantum Wells. Phys. Rev. Lett. **76**, 3308 (1996)
26. R. Graham, Squeezing and frequency changes in harmonic oscillations. J. Mod. Optics **34**, 873 (1987)
27. R. Grauer, B. Birnir, The center manifold and bifurcations of damped and driven sine-Gordon breathers. Phys. D Nonlinear Phenom. **56**, 165 (1992)
28. J. Guckenheimer, P. Holmes, *Nonlinear oscillations, dynamical systems, and bifurcations of vector fields* (Springer, New York, 1983)
29. J.N. Heyman et al., Resonant harmonic generation and dynamics screening in a double quantum well. Phys. Rev. Lett. **72**, 2183 (1994)
30. J.N. Heyman et al., Temperature and intensity dependence of intersubband relaxation rates from photovolgate and absorption. Phys. Rev. Lett. **74**, 2682 (1995)
31. Y. Huang, W. Li, W. Ma, H. Qin, Y. Zhang, Experimental observation of spontaneous chaotic current oscillations in GaAs/Al0.45Ga0.55As superlattices at room temperature. Chin. Sci. Bull. **57**, 2070 (2012)
32. Y. Huang, W. Li, W. Ma, H. Qin, H.T. Grahn, Y. Zhang, Spontaneous quasi-periodic current self-oscillations in a weakly coupled GaAs/(Al, Ga)As superlattice at room temperature. Appl. Phys. Lett. **102**, 242107 (2013)
33. I. Kanter, Y. Aviad, I. Reidler, E. Cohen, M. Rosenbluth, An optical ultrafast random bit generator. Nat. Photonics **4**, 58 (2010)

34. J. Kastrup, R. Hey, K.H. Ploog, H.T. Grahn, L.L. Bonilla, M. Kindelan, M. Moscoso, A. Wacker, J. Galán, Electrically tunable GHz oscillations in doped GaAs-AlAs superlattices. Phys. Rev B. **55**, 2476 (1997)
35. E.W. Laedke, K.H. Spatschek, On localized solutions in nonlinear faraday resonance. J. Fluid Mech. **223**, 589–601 (1991)
36. K. Leo, P.H. Bolivar, F. Brüggemann, R. Schwedler, K. Klaus, Köhler, Observation of Bloch oscillations in a semiconductor superlattice. Solid State Commun. **10**, 943–946 (1992)
37. W. Li, I. Reidler, Y. Aviad, Y.Y. Huang, H. Song, Y.H. Zhang, M. Rosenbluh, I. Kanter, Fast physical random-number generation based on room-temperature chaotic oscillations in weakly coupled superlattices. Phys. Rev. Lett. **111**, 044102 (2013)
38. C.M. Morris, Interplay of quantum confinement, electron-electron interactions, and terahertz radiation in indium gallium arsenide quantum posts and gallium arsenide quantum wells. Ph.D. thesis, University of California, Santa Barbara, 2011
39. T.E. Murphy, R. Roy, The world's fastest dice. Nat. Photonics **2**, 714–715 (2008)
40. M.A. Nielsen, I.L. Chuang, *Quantum Computation and Quantum Information* (Cambridge University Press, Cambridge, UK, 2000)
41. I. Reidler, Y. Aviad, M. Rosenbluh, I. Kanter, Ultrahigh-speed random number generation based on a chaotic semiconductor laser. Phys. Rev. Lett. **103**, 024102 (2009)
42. M. Ruiz-Garcia, J. Essen, M. Carretero, L.L. Bonilla, B. Birnir, Enhancing chaotic behavior at room temperature in GaAs/(Al, Ga)As superlattices. Phys. Rev. B **95**, 085204 (2017)
43. A.K. Saxena, The conduction band structure and deep levels in Ga1-xAlxAs alloys from a high-pressure experiment. J. Phys. C Solid State Phys. **23**, 4323 (1980)
44. M. Sciamanna, K.A. Shore, Physics and applications of laser diode chaos. Nat. Photonics **9**, 151–162 (2015)
45. D.R. Stinson, *Cryptography: Theory and Practice*, 3rd edn. (CRC Press, Boca Raton, 2006)
46. A. Uchida, K. Amano, M. Inoue, K. Hirano, S. Naito, H. Someya, I. Oowada, T. Kurashige, M. Shiki, S. Yoshimori, K. Yoshimura, P. Davis, Fast physical random bit generation with chaotic semiconductor lasers. Nat. Photonics **2**, 728–732 (2008)
47. J.Q. Wu, D.S. Jiang, B.Q. Sun, Room-temperature microwave oscillation in alas/gaas superlattices. Phys. E Low-dimensional Syst. Nanostruct. **4**(2), 137–141 (1999)
48. Z. Yin, Y. Zhang, M. Ruiz-García, M. Carretero, L.L. Bonilla, K. Biermann, H.T. Grahn, Noise-enhanced chaos in a weakly coupled GaAs/(Al,Ga)As superlattice (unpublished)
49. M. Zalużny, Influence of the depolarization effect on the nonlinear intersubband absorption spectra of quantum wells. Phys. Rev. B **47**, 3995 (1993)
50. M. Zalużny, Saturation of intersubband absorption and optical rectification in asymmetric quantum wells. J. Appl. Phys. **74**, 4716 (1993)